*R*esearch in
*A*stronomy and
*A*strophysics

CO observations of the Galactic bubble N4 *

Jun-Yu Li[1,2], Zhi-Bo Jiang[1], Yao Liu[1] and Yuan Wang[1]

[1] Purple Mountain Observatory, Chinese Academy of Sciences, Nanjing 210008, China; *lijunyu@pmo.ac.cn*
[2] University of Chinese Academy of Sciences, Beijing 100049, China

Abstract We present a study of the Galactic bubble N4 using the 13.7 m millimeter-wave telescope, which is managed by Purple Mountain Observatory at Qinghai Station. N4 is one of the science demonstration regions where simultaneous observations of ^{12}CO ($J = 1 - 0$), ^{13}CO ($J = 1 - 0$) and C^{18}O ($J = 1 - 0$) line emission towards N4 were carried out under the project Milky Way Imaging Scroll Painting (MWISP). We analyze the spectral profile and the distribution of the molecular gas. Morphologically, the CO emissions correlate well with Spitzer IRAC 8.0 μm emission. The channel map and velocity-position diagram show that N4 is more likely to be an inclined expanding ring rather than a spherical bubble. We calculated the physical parameters of N4 including mass, size, column density and optical depth. Some massive star candidates were discovered in the region of N4 using the (J, $J-H$) color-magnitude diagram. We found a candidate for the energy source driving the expansion of N4, a massive star with a mass of $\sim 15\,M_\odot$ and an age of ~ 1 Myr. There is the signature of infall motion in N4, which can be a good candidate for the infall area. Combining millimeter and infrared data, we suggest that triggered star formation can exist in N4.

Key words: ISM: bubbles — ISM: clouds — molecules — stars: formation

1 INTRODUCTION

The Galactic bubble N4 ($l = 11.892°$ and $b = 0.748°$) was first revealed in the Galactic Legacy Infrared Mid-Plane Survey Extraordinaire (GLIMPSE; Benjamin et al. 2003; Churchwell et al. 2009) by the Spitzer telescope. N4 is surrounded by a shell of accumulated material (Deharveng et al. 2010). The distance to N4 ($d = 3.2$ kpc) has been determined from the radial velocity of an over-lapping HII region (Churchwell et al. 2006). Since the probability of chance alignments for the HII region with a bubble is quite small ($< 1\%$) (Churchwell et al. 2006), we assume that the bubble lies at the same distance as the HII region. The bubble at the far kinematic distance (13.4 kpc) would be so far away that only the near distance is a realistic choice, therefore in this paper the near distance, i.e. 3.2 kpc, is adopted as the distance of N4.

The strong winds and radiation fields from massive stars clear out large cavities in the interstellar medium (ISM). These cavities (or bubbles) impact their surrounding molecular clouds and may influence the formation of stars therein (Beaumont & Williams 2010). At the boundaries of these

---

bubbles lies the material, displaced by the propagating wind or ionization front. Such a dynamic process, which alters the physical environment of molecular clouds, might trigger the formation of a new generation of stars.

The study of the bubbles can give some information about the stellar winds that produce them and the structure and physical properties of the ambient ISM into which they are expanding. Thus the distribution of dense molecular material can reflect the interaction between the bubble and its surrounding molecular clouds. It is speculated that gravitational collapse might be triggered by the expanding bubble when the leading shock front overruns and compresses a preexisting molecular cloud, resulting in star formation. In theory, stars with all masses can form in the shell around an HII region. Small-scale gravitational instabilities (for example Jeans instabilities) can lead to the formation of low-mass stars; large-scale gravitational instabilities along the collected shell can lead to the formation of massive fragments, potential sites of massive star formation; this is called the "collect and collapse" process (Elmegreen & Lada 1977).

In order to study the interaction between the bubble and ambient molecular clouds, we observed the molecular clouds associated with N4. So far there has been little information compiled about the molecular clouds around N4. Although continuum imaging of dust in infrared and sub-mm can easily identify a bubble morphologically, observations of molecular lines are crucial for searching for kinematic evidence of interactions between HII regions and molecular clouds and testing the theory supporting the collect and collapse process. Therefore observations of CO (^{12}CO , ^{13}CO, C^{18}O) line emissions towards N4 were done simultaneously.

The observations and data reduction are described in Section 2; the results and data analysis are presented in Section 3; Section 4 is the discussion and Section 5 is the conclusions.

2 OBSERVATIONS AND DATA REDUCTION

The observations of N4 were carried out from 2011 December 24 to December 26 as a part of the Multi-Line Galactic Plane Survey of CO and its isotopic transitions, also called the Milky Way Imaging Scroll Painting (MWISP; *http://www.radioast.nsdc.cn/yhhjindex.php*). This is a project dedicated to the large-scale survey of dense molecular gas along the northern Galactic plane. Regions within the Galactic range of $-5.25° \leq b \leq 5.25°$, $-10.25° \leq l \leq 250.25°$ and some other interesting areas are divided into $\sim$11 000 units in a grid of (l, b), with each unit having a size of $30' \times 30'$. The Superconducting Spectroscopic Array Receiver (SSAR) is used, which is a superconducting focal plane array that observes a 3×3 beam and is mounted on the Delingha 13.7 m millimeter-wave telescope (Shan et al. 2012 [1]; Zuo et al. 2011). The array receiver was made by Superconductor-Insulator-Superconductor (SIS) mixers that use the sideband separation scheme. A specific local oscillator frequency was selected so that the upper sideband is centered at the ^{12}CO (1−0) line and the lower sideband covers the ^{13}CO (1−0) and C^{18}O (1−0) lines, which enable us to make simultaneous detection of the CO isotopic lines. The back end is a Fast Fourier Transform Spectrometer (FFTS) that has 16 384 channels with a bandwidth of 1000 MHz and an effective spectral resolution of 61.0 kHz (0.16 km s^{-1}). The size of the main beam is about $52''$ at 115 GHz and the main beam efficiency η_{mb} is 0.46 at the upper sideband and 0.43 at the lower sideband. The absolute pointing uncertainty was estimated to be $\sim 5''$, which was derived from continuum observations of planets. Using On-The-Fly (OTF) scanning, with a scanning rate of $75''$ per second and a total integration time of 54 s per pixel, a large region ($-1° \leq b \leq 1°$, $12.5° \leq l \leq 16°$) has been observed, but in this work we take a smaller region ($\sim 21.6' \times 21.6'$) as the main target. During the observation, we took spectra of the standard source W51D every two hours to ensure that the telescope and the other devices were working properly. We used the standard chopper wheel calibration technique to measure antenna temperature T_A^* corrected for atmospheric absorption. The final data were recorded on

---

[1] *http://ieeexplore.ieee.org/xpl/login.jsp?tp=&arnumber =6313968&url=http%3A%2F%2Fieeexplore.ieee.org%2Fxpls %2Fabs_all.jsp%3Farnumber%3D6313968*

a brightness temperature scale of T_R^* (K). The system temperatures were about $250 - 350$ K during the observation.

The spectral data were reduced and analyzed with the GILDAS/CLASS[2] package. As a preliminary step in data reduction, all spectra of nine beams were individually inspected and those with either strongly distorted baselines or abnormal root mean square (rms) noise levels were discarded. We combined the spectra at the same positions and subtracted the linear baseline from the adopted spectra. The rms was about 0.48 K for ^{12}CO and 0.27 K for ^{13}CO and C^{18}O.

3 RESULTS AND DATA ANALYSIS

3.1 The Morphologies Illustrated by the ^{12}CO $(1-0)$, ^{13}CO $(1-0)$ and C^{18}O $(1-0)$ Emission

Figure 1 shows the velocity-integrated CO emission, which we call W_{CO}(K km s^{-1}). In the maps of W_{CO}, the red circle indicates the position of the N4 region ($\sim 7.2' \times 7.2'$). We can see that the molecular CO emissions from N4 are almost circular. The most striking feature of the CO data is the rarity of emission toward the center of N4. The maps of W_{CO} also show clumpy structures along the shell of N4. This suggests that the physical conditions (temperature, density) are not uniform in N4. The emission of ^{12}CO and ^{13}CO is strong, but the C^{18}O emission is weak. We take contour levels starting at 30% ($\sim$36 K km s^{-1}) of the peak ^{12}CO integrated intensity, with a step of $\sim$12 K km s^{-1} in the top left panel; contour levels start at 30% ($\sim$12 K km s^{-1}) of the peak ^{13}CO integrated intensity, with a step of ~ 4 K km s^{-1} in the top right panel; contour levels start at 5σ ($\sigma \sim$0.34 K km s^{-1}) of the C^{18}O integrated intensity, with a step of ~ 0.57 K km s^{-1} in the bottom panel. As one advances through velocity space and the spectral lines of CO emission, there are several components in the line of sight. The emission from N4 has a velocity range of 21 km s^{-1} $< V_{LSR} <$ 28 km s^{-1}. Thus the integrated velocity range from the three panels is entirely in the range 21 km s^{-1} to 28 km s^{-1}.

3.2 The Infrared Dust and CO Distribution of N4

In Figure 2, we present maps where the ^{12}CO, ^{13}CO and C^{18}O data are overlaid on the infrared data. The data of N4 from Spitzer IRAC 8.0 μm and CO emissions taken with the 13.7 m telescope show that the HII region is surrounded by a remarkably complete ring. According to Churchwell et al. (2006), bubbles found in GLIMPSE are generally detectable in all four IRAC bands but tend to be brighter at longer wavelengths. Most bubbles are larger and brighter at 8.0 μm than at the shorter wavelength. This is also the case for N4. The 8.0 μm emission is faint or absent inside the bubble, but bright along the shell that defines the bubble, and generally extends well beyond the bubble's shell boundary. Churchwell et al. (2006) postulated that the 8.0 μm band emission is probably dominated by the 7.7 μm and 8.6 μm features attributed to polycyclic aromatic hydrocarbons (PAHs). The fact that 8.0 μm emission appears to be essentially absent in the central regions of the bubbles (the front and back sides of the shell that defines the bubble contribute some emission) implies that PAHs are either easily destroyed in the hard radiation field of the central star(s) or blown out of the central regions by stellar winds.

In Figure 2, the CO emissions are clearly associated with the 8.0 μm emission; their morphology is similar, especially that shown by the C^{18}O emission. The CO emissions are faint in the central regions of N4. Also, Figure 2 shows that the distribution of ^{12}CO and ^{13}CO is wider than the distribution of PAHs. There are some possible reasons for this. First, the critical density of C^{18}O is the highest, ^{13}CO is lower and ^{12}CO is the lowest. ^{12}CO traces diffuse molecular gas, but C^{18}O traces dense molecular gas. Therefore the distribution of ^{12}CO is much wider than that of C^{18}O. Second, PAH emission originates from Photo Dissociation Regions. PAHs trace warm regions, but CO traces cold regions. Therefore, there is much more CO gas than PAHs.
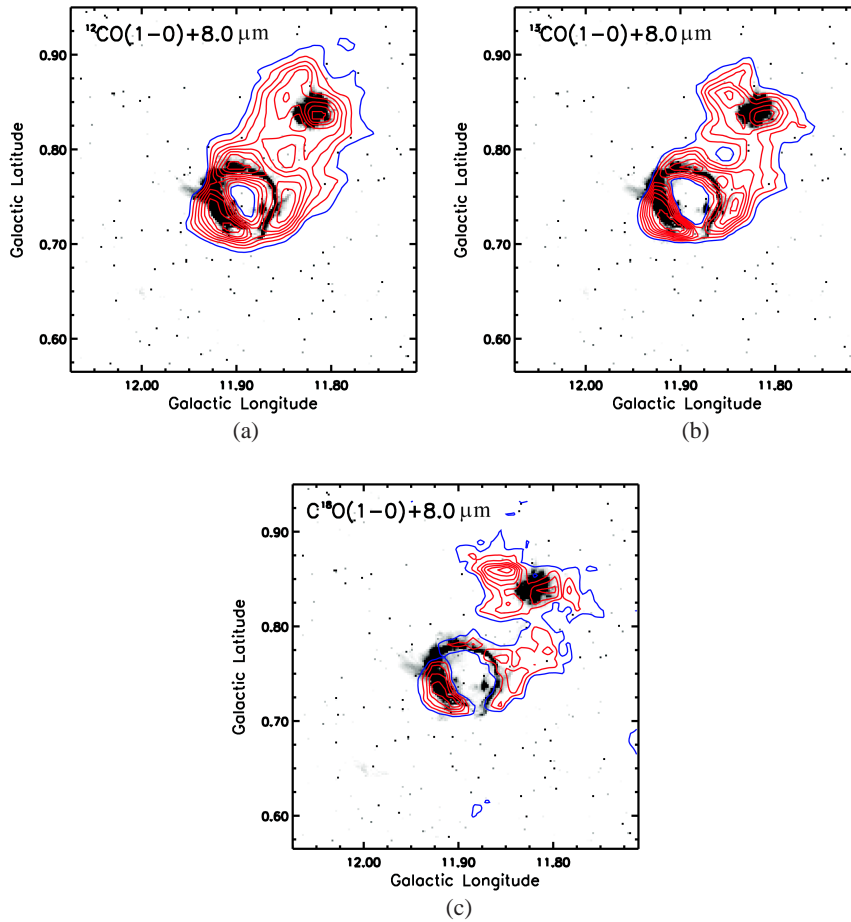
---

[2] *http://iram.fr/IRAMFR/GILDAS/*
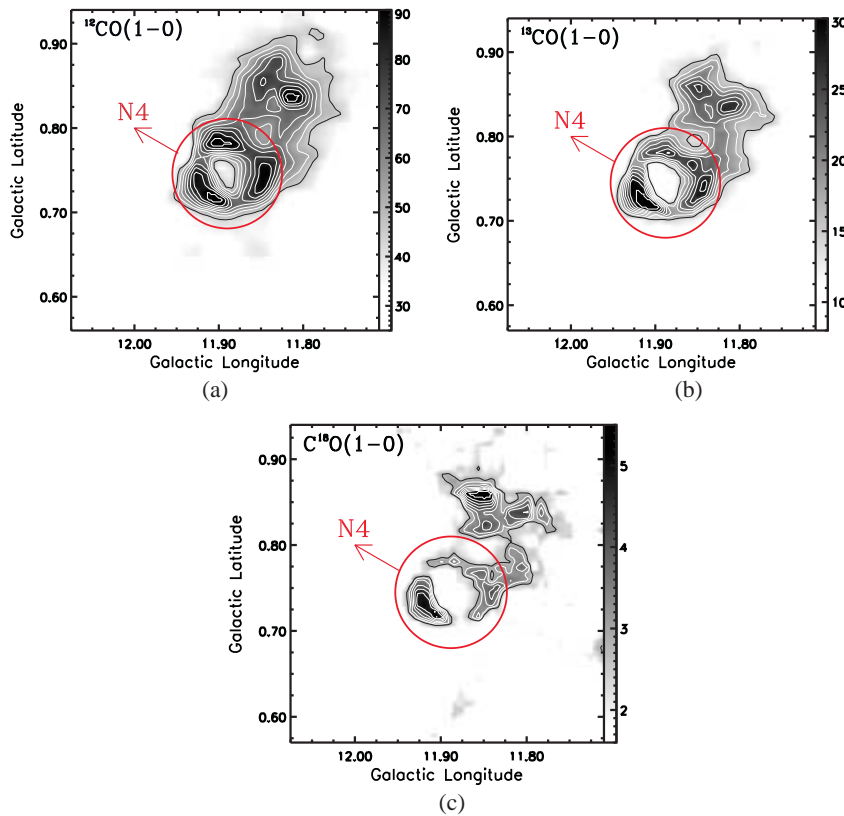
Fig. 1 (a) The integrated intensity map of ^{12}CO. Contour levels start at 30% ($\sim$ 36 K km s^{-1}) of the peak ^{12}CO integrated intensity, with a step of $\sim$ 12 K km s^{-1}. (b) The integrated intensity map of ^{13}CO. Contour levels start at 30% ($\sim$ 12 K km s^{-1}) of the peak ^{13}CO integrated intensity, with a step of $\sim$ 4 K km s^{-1}. (c) The integrated intensity map of C^{18}O. Contour levels start at 5σ ($\sigma \sim$ 0.34 K km s^{-1}) of the C^{18}O integrated intensity, with a step of $\sim$ 0.57 K km s^{-1}. The integrated velocity range is all from 21 km s^{-1} to 28 km s^{-1}. The red circle indicates the position of N4. The unit of the shaded bar is in K km s^{-1}.

3.3 The Velocity Structure of N4

More detailed information about emission is shown in Figure 3. Each panel shows a map of $W_{\rm CO}$ for ^{13}CO emission with different values of velocity displayed in the upper left corner. The morphology of the emissions in different channels follows a sequence where the ^{13}CO emission of N4 first appears in the southwest direction, then enlarges and becomes a semicircle, a circle, then again a semicircle, and finally disappears in the northeast direction.

Figure 3 indicates that the southwest part is blueshifted, while the northeast part is redshifted. As one advances through the measured velocity values, a spherical shell would appear as a small blueshifted region (the front cap of the bubble), expand into a ring (the midsection of the bubble), and then contract back to a small redshifted region (the back cap of the bubble) (Arce et al. 2011). If bubbles are two dimensional projections of spherical shells, we can expect to see the front and back faces of these shells at blueshifted and redshifted velocities (Beaumont & Williams 2010). Therefore if N4 is an expanding bubble, having a spherical shape, the channel map of ^{13}CO emission would appear different from that shown in Figure 3. However, with an inclined expanding ring, we would

Fig. 2 (a) ^{12}CO integrated intensity contours (for 21 km s^{-1} < V_{LSR} < 28 km s^{-1}) overlaid on a Spitzer IRAC 8.0 μm image of N4 from the GLIMPSE. Contour levels start at 30% ($\sim$ 36 K km s^{-1}) of the peak ^{12}CO integrated intensity, with a step of $\sim$ 12 K km s^{-1}. (b) ^{13}CO integrated intensity contours (for 21 km s^{-1} < V_{LSR} <28 km s^{-1}) overlaid on an 8.0 μm image. Contour levels start at 30% ($\sim$ 12 K km s^{-1}) of the peak ^{13}CO integrated intensity, with a step of $\sim$ 4 K km s^{-1}. (c) C^{18}O integrated intensity contours (for 21 km s^{-1} < V_{LSR} < 28 km s^{-1}) overlaid on an 8.0 μm image. Contour levels start at 30% ($\sim$ 1.65 K km s^{-1}) of the peak C^{18}O integrated intensity, with a step of $\sim$ 0.55 K km s^{-1}.

expect the observed channel map like that shown in Figure 3. In such a case, the front part of the inclined ring moves toward us (blueshift), and its back part moves away from us (redshift). Thus N4 is more likely to be an inclined expanding ring than a spherical bubble.

There may be other possibilities, for example, one of the most natural interpretations to draw from this observation is that the front and back of N4 are missing, and we are instead observing only the bubble's midsection. A corollary of this conclusion is that the molecular clouds, in which N4 is embedded, are oblate with a thickness of a few parsecs, comparable to the typical diameter of a ring. In this scenario, N4 expands and escapes from the molecular clouds along its axis and we see a ring of CO emission, approximately circular if the flattened axis is along our line of sight; otherwise it is
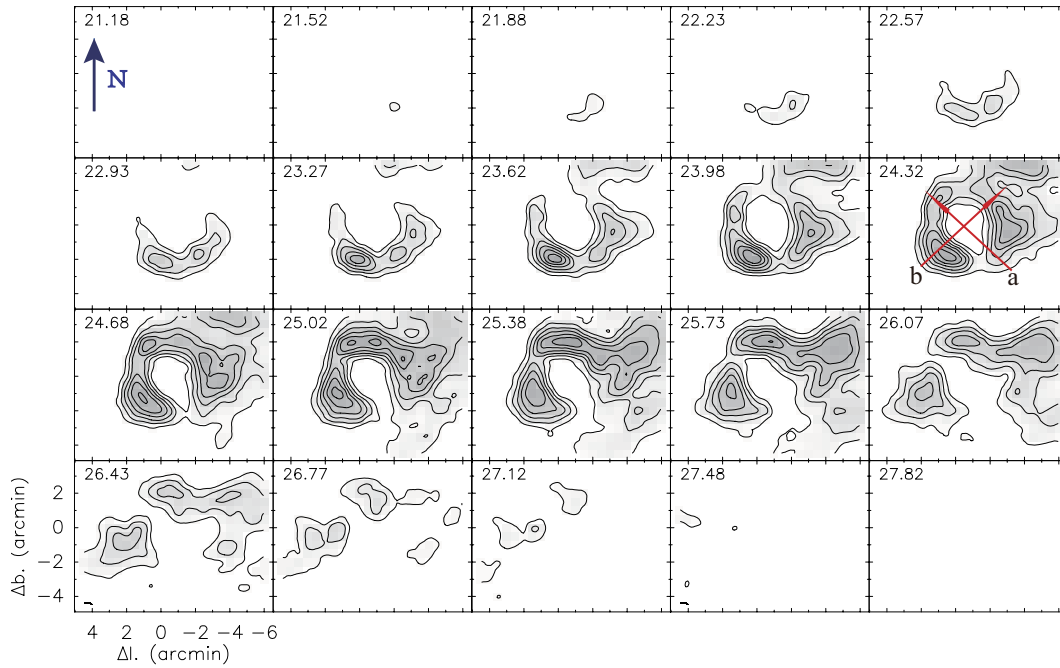
Fig. 3 The channel map of W_{CO} integrated over two channels (for 21 km s^{-1} < V_{LSR} < 28 km s^{-1}). Contour levels start at 40% (∼ 16 K km s^{-1}) of the peak ^{13}CO (1−0) integrated intensity, with a step of ∼ 0.55 K km s^{-1}. The number in the upper left corner of each panel indicates the central V_{LSR} of the channel map. The coordinate is relative to the center of N4 (11.892°, 0.748°). Arrows a and b are labeled as the directions we define on the velocity-position map.

elliptical. This kind of situation could happen, since the densities of molecular clouds are different in the front, middle and back parts of the bubble. In any case, we would like to believe that N4 has a ring structure, no matter if it is actually a ring or a bubble that has no front or back.

3.4 The Kinematics of N4 in ^{13}CO (1−0) Emission

In order to study more detailed information about the kinematics of N4, we make a velocity-position map of the ^{13}CO emission. To draw this map, we define two directions which are labeled as a (the northeast direction) and b (the northwest direction), as shown in Figure 3. Direction a is taken from the southwest point (the smallest velocity) to the center of N4 and extended to the outer boundary of N4; direction b is taken perpendicularly to direction a.

Figure 4 shows the velocity-position map of the ^{13}CO emission of N4. The two red lines plotted on the two panels represent the velocity of the molecular clouds in the vicinity of N4, which with a value of ∼ 24.3 km s^{-1} is used as an indicator of the system velocity of the local molecular clouds. Also we draw six points in each panel to show the central velocity of the inner, the middle and the outer point along each cut (a, b). The diagonal arrow plotted in panel (a) shows a trend that the velocity in the southwest part of N4 is smaller than in the northeast part, i.e., N4 has a blueshift and redshift in the direction a. Two panels also show that the velocity of the inner region (blue point) is smaller than the velocity of the outer region (red point).
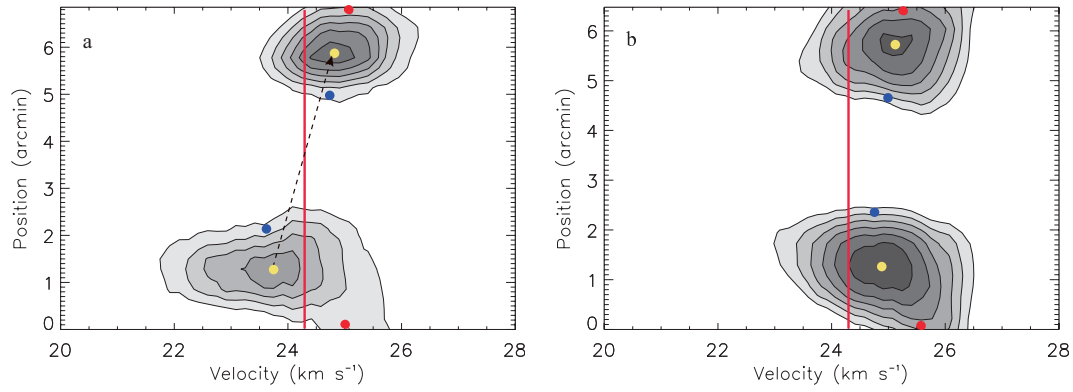
Fig. 4 The velocity-position map of the ^{13}CO emission of N4. The two panels represent two directions (a, b) taken which is a cross shown in Fig. 3. The two red lines plotted on the two panels show the velocity of the molecular clouds in the vicinity of N4, which is used as an indicator of system velocity of the local molecular clouds, the value of which is ~ 24.3 km s^{-1}. Six points in each panel show the central velocity of the inner, the middle and the outer point along each cut (a, b). The contour levels are from 0.8 K to 4.2 K in steps of ~ 0.6 K.
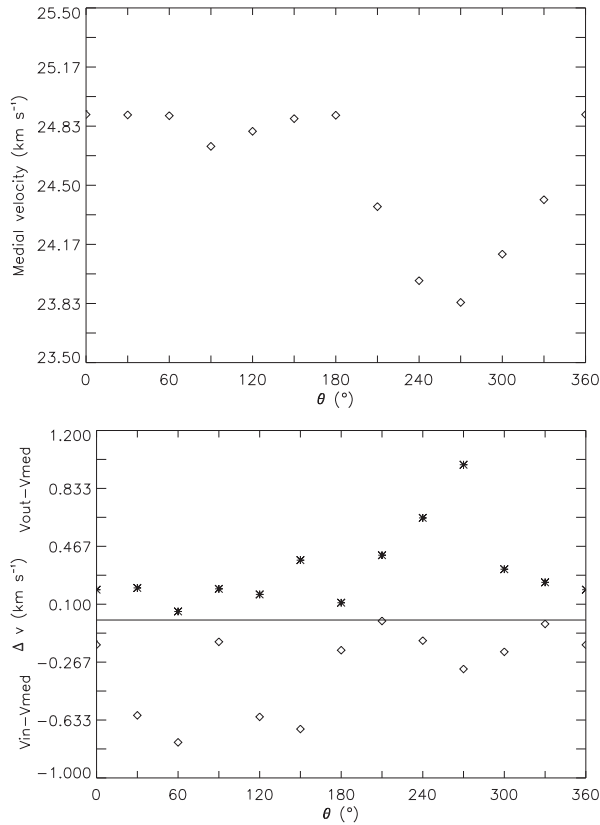
Fig. 5 The velocity-theta plot of the ^{13}CO emission of N4. V_{in} is the velocity of the inner circle of N4, and V_{out} is the velocity of the outer circle of N4. V_{med} is the velocity of the middle circle of N4.

To verify if all directions in N4 have this same property, we draw a velocity-theta plot. Theta is the angle that starts from $0°$(direction b) and increases in the counterclockwise direction. We make three circles (the inner circle, the middle circle, the outer circle) and some radial lines start at the center of N4 with a step of $30°$, so each radial line crosses a circle three times. We calculate the average velocity at the crosses and name them V_{in}, V_{med} and V_{out}, corresponding to the inner, middle and outer circles respectively.

Figure 5 shows the velocity-theta plot of the ^{13}CO emission of N4. In Figure 5, the left panel shows V_{med} at $0° < \theta < 180°$ is larger than V_{med} at $180° < \theta < 360°$, suggesting the same conclusion as previously stated, that the southwest part of N4 has a blueshift and the northeast part of N4 has a redshift. The right panel shows $V_{out} - V_{med} > 0$ (for $0° < \theta < 360°$) and $V_{in} - V_{med} < 0$ (for $0° < \theta < 360°$). This means that for N4, $V_{in} < V_{out}$ in all directions. This kind of phenomenon suggests N4 may have a twisting motion. Because the resolution of the 13.7 m millimeter-wave telescope is not good enough, we regard this kind of motion as being marginally detected. Higher resolution observations are necessary to confirm this.

3.5 Infall Motion in N4

Gravitational infall or core collapse can take place in high-mass young stellar objects (YSOs) at early stages and continue all the way to the stage of Ultra Compact HII regions (Keto 2003; Sollins & Ho 2005). Many infall candidates have been identified based on their spectral signature. They can serve as good targets to study the birth of massive stars and gas dynamics in molecular cores (e.g. Ren et al. 2012). For the ^{12}CO emission, the blueshifted emission peak is stronger than the redshifted one, and the central absorption dip coincides well with the ^{13}CO or $C^{18}O$ line peak. Such a blue asymmetric ^{12}CO line suggests the presence of infall motion towards the core's center in the molecular cloud. When infall occurs in the envelope, where the outer region is cooler than the inner region, the gas in the front part (outer region) would absorb the redshifted emission, leaving a dip on the redshifted side (Zhou et al. 1993; Mardones et al. 1997).

In N4, when we checked the spectra of the ^{12}CO emission, we found one region shows this blue asymmetric signature. As shown in Figure 6, we located the center position ($l = 11.92°$, $b = 0.74°$), then recorded observations of 20 ($5×4$) positions nearby the center to analyze spectra from ^{12}CO, ^{13}CO and $C^{18}O$. We can see there are seven or eight positions that have this feature, i.e. blue asymmetry. Therefore it can be an infall candidate. However there are many components along the line of sight. The spectra are complex, and the resolution of the 13.7 m telescope is not sufficient, so we need higher resolution observations to confirm if this is infall motion.

3.6 The Spectra of ^{12}CO (1−0), ^{13}CO (1−0) and $C^{18}O$ (1−0)

The entire emission profiles of ^{12}CO, ^{13}CO and $C^{18}O$, averaged over the entire region of N4 (the red circle), are shown in Figure 7. The blue line represents the ^{12}CO emission, green the ^{13}CO emission and red the $C^{18}O$ emission. We see the emission of ^{12}CO is multi-peaked, indicative of several components along the line of sight. The emission from N4 is the main peak with a velocity range of $21\ km\ s^{-1} < V_{LSR} < 28\ km\ s^{-1}$. The peak brightness temperature T_R^* of ^{12}CO, ^{13}CO and $C^{18}O$ is ~ 15.5, 5 and 1 K, respectively.

3.7 The Physical Parameters of N4

By Gaussian fitting the spectral lines of ^{12}CO, ^{13}CO and $C^{18}O$, we obtained some parameters. Since the spectral lines of N4 are multi-peaked (Fig. 7), the parameters of the main peak are adopted (see Table 1).
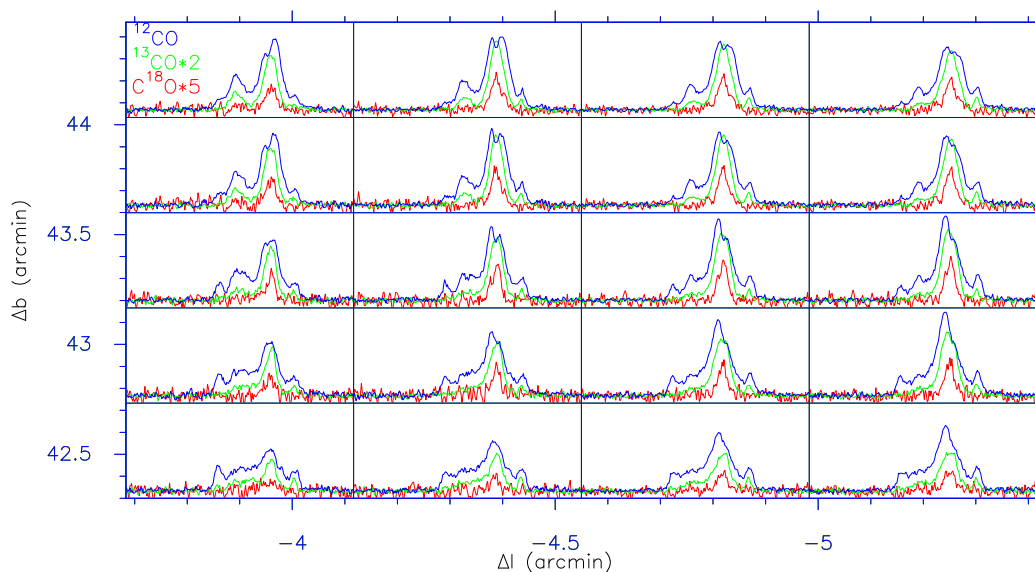
Fig. 6 The blue line is ^{12}CO emission, the green line is ^{13}CO emission and the red line is C^{18}O emission. The brightness temperature of each ^{13}CO spectrum is multiplied by two and the brightness temperature of each C^{18}O spectrum is multiplied by five. The coordinate is expressed relative to $l = 12.0°$ and $b = 0°$.
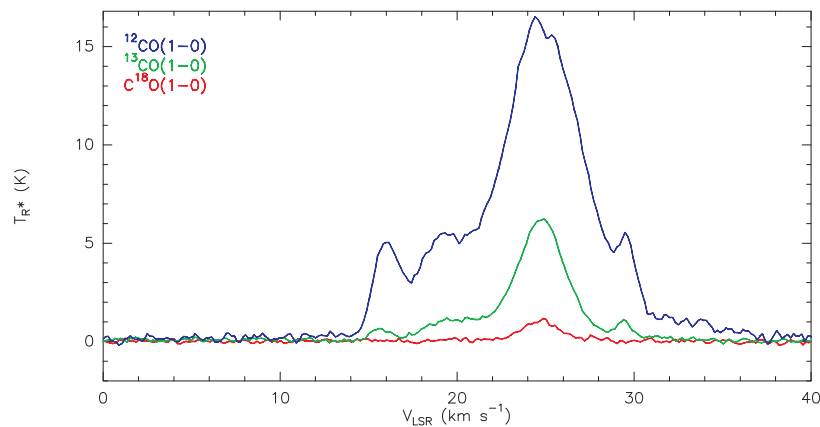
Fig. 7 The spectral lines of ^{12}CO (1−0), ^{13}CO (1−0) and C^{18}O (1−0), averaged over the entire region of N4.

Table 1 Fundamental Parameters of CO Emission

^{12}CO (1−0)			^{13}CO (1−0)			C ^{18}O (1−0)		
T_R^*(peak)	Width	Velocity	T_R^*(peak)	Width	Velocity	T_R^*(peak)	Width	Velocity
(K)	(km s^{-1})	(km s^{-1})	(K)	(km s^{-1})	(km s^{-1})	(K)	(km s^{-1})	(km s^{-1})
15.1	5.1	24.7	4.4	2.9	24.7	0.8	2.8	24.7

Table 2 Derived Physical Parameters of N4

Parameter	^{13}CO	C^{18}O
A_i (pc^2)	32.4	10.2
T_{ex} (K)	18.6	18.6
τ	0.35	0.058
N(CO) (cm^{-2})	1.6×10^{16}	3.0×10^{15}
N(H$_2$) (cm^{-2})	1.1×10^{22}	2.1×10^{22}
$M(M_\odot)$	7.0×10^3	4.3×10^3

Here we assume that the molecular clouds are in Local Thermodynamic Equilibrium and the line center of ^{12}CO (1−0) is optically thick. Using the formula given by Rohlfs & Wilson (2000) and Nagahama et al. (1998), the physical parameters of N4 are calculated.

$$T_{\mathrm{ex}} = \frac{5.53}{\ln\left(1 + \frac{5.53}{T_{\mathrm{R}}^*(^{12}\mathrm{CO}) + 0.82}\right)}, \tag{1}$$

where T_{R}^* is the brightness temperature, and we can obtain the excitation temperature of ^{12}CO (1−0), $T_{\mathrm{ex}} = 18.6$ K. Assuming that ^{13}CO (1−0) and C^{18}O (1−0) have the same excitation temperature as ^{12}CO (1−0), the optical depth of ^{13}CO and C^{18}O can be calculated using (2) and (3):

$$\tau(^{13}\mathrm{CO}) = -\ln\left(1 - \frac{T_{\mathrm{R}}^*(^{13}\mathrm{CO})}{\frac{5.29}{\exp(5.29/T_{\mathrm{ex}}-1)} - 0.89}\right), \tag{2}$$

$$\tau(\mathrm{C}^{18}\mathrm{O}) = -\ln\left(1 - \frac{T_{\mathrm{R}}^*(\mathrm{C}^{18}\mathrm{O})}{\frac{5.27}{\exp(5.27/T_{\mathrm{ex}}-1)} - 0.89}\right). \tag{3}$$

The column density of ^{13}CO and C^{18}O can be obtained using (4) and (5):

$$N(^{13}\mathrm{CO}) = 4.57 \times 10^{13}(T_{\mathrm{ex}} + 0.89)\exp(5.29/T_{\mathrm{ex}})\int T_{\mathrm{R}}^*(^{13}\mathrm{CO})dv, \tag{4}$$

$$N(\mathrm{C}^{18}\mathrm{O}) = 4.57 \times 10^{13}(T_{\mathrm{ex}} + 0.89)\exp(5.27/T_{\mathrm{ex}})\int T_{\mathrm{R}}^*(\mathrm{C}^{18}\mathrm{O})dv. \tag{5}$$

Assuming $N(\mathrm{H}_2)/N(^{13}\mathrm{CO}) = 7 \times 10^5$ (Nagahama et al. 1998) and $N(\mathrm{H}_2)/N(\mathrm{C}^{18}\mathrm{O}) = 7 \times 10^6$ (Castets & Langer 1995), where $N(\mathrm{H}_2)$ is the average column density of the hydrogen molecules, the mass of the molecular cloud can be obtained as

$$M = \mu m_{\mathrm{H}} \sum (N(\mathrm{H}_2)_i \cdot A_i)/2 \times 10^{30} \quad (M_\odot), \tag{6}$$

where $\mu = 2.8$ is the mean molecular weight, m_{H} is the mass of a hydrogen atom and A_i is the projected area of the ^{13}CO or C^{18}O emission region. Detailed information is shown in Table 2.

Because C^{18}O traces denser molecular gas than ^{13}CO, A_i (C^{18}O) is smaller than A_i (^{13}CO). The C^{18}O is optically thin, but ^{13}CO is optically thick relative to C^{18}O. Therefore the mass of N4 derived from the ^{13}CO emission is larger than the mass derived from the C^{18}O emission at the assumed distance $d = 3.2$ kpc. Thus we suggest the mass of N4, i.e. $\sim 7.0 \times 10^3 \, M_\odot$, is more correct. Deharveng et al. (2010) have noted that N4 is surrounded by a shell of collected material, and its mass is about 1150 $M_\odot$ at $d = 3.14$ kpc. They use the 870 μm cold dust emission to estimate the amount of neutral material associated with N4. Because the dust continuum traces much more dense gas than ^{13}CO and C^{18}O, the projected areas of ^{13}CO and C^{18}O emissions are larger than the 870 μm cold dust emission. Therefore it is reasonable that the mass of N4 we calculated is larger than that of Deharveng et al. (2010).

4 DISCUSSION

4.1 Energy Source for N4

The infrared dust bubble may be produced by exciting O- or B-type star(s), which are located inside the bubble. The ultraviolet (UV) radiation from exciting star(s) may heat dust and ionize the gas to form an expanding bubble shell (Watson et al. 2008). There are many stars inside and along the shell of N4. From the 2MASS (Skrutskie et al. 2006) point source catalog, the $(J, J-H)$ color-magnitude diagram is made, which is shown in Figure 8. The solid line represents the locus of the main sequence stars (Covey et al. 2007). Several point sources which are located above the dashed line are regarded as candidates of massive stars. We find a candidate of a massive star near the central region of N4, labeled as S1, shown in Figure 9. We compile the photometries available at different wavelengths (JHK + IRAC + WISE 12 μm + WISE 22 μm) for this candidate S1, see Figure 10. Using standard models for circumstellar disks (e.g., Liu et al. 2012) and the well-tested radiative transfer code MC3D (Wolf 2003), we performed an SED fitting to derive the properties of this source. The results are shown in Figure 10. The luminosity and the effective temperature of the best-fitting model are $\sim$25 000 $L_\odot$ and $\sim$20 000 K respectively. Interpolation of the pre-main sequence stellar models presented by Bernasconi (1996) suggests that S1 is a massive young stellar object with a mass of $\sim$15 $M_\odot$ and an age of $\sim$ 1 Myr. It correlates with the result shown in Figure 8. A massive star (15 $M_\odot$) with an age of a million years can produce energy $\sim$2.6 × 10^{44} J in the UV band whereas the kinematic energy ($E = 1/2Mv^2$) of N4 is estimated to be $\sim$1.4 × 10^{39} J, implying that the UV photons produced by a massive star in 1 Myr are sufficient to drive the expansion of N4. Because of the position, age and energy output of S1, we think S1 may be the energy source for the expansion of N4, which deserves further studies.
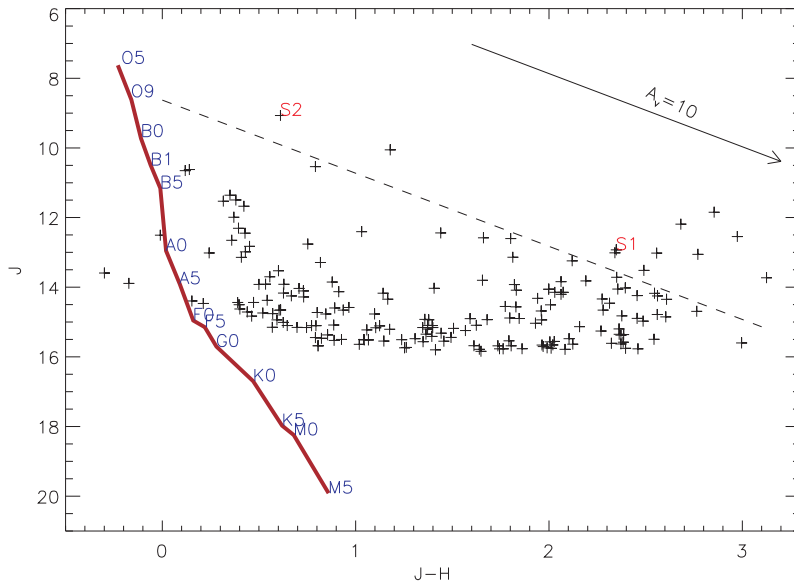
Fig. 8 The $(J, J-H)$ color-magnitude diagram for the stars in the N4 region. The solid line represents the locus of the main sequence stars. The plotted arrow represents the extinction vector. The dashed line is parallel to the extinction vector and is drawn from where O9 appears on the main sequence.
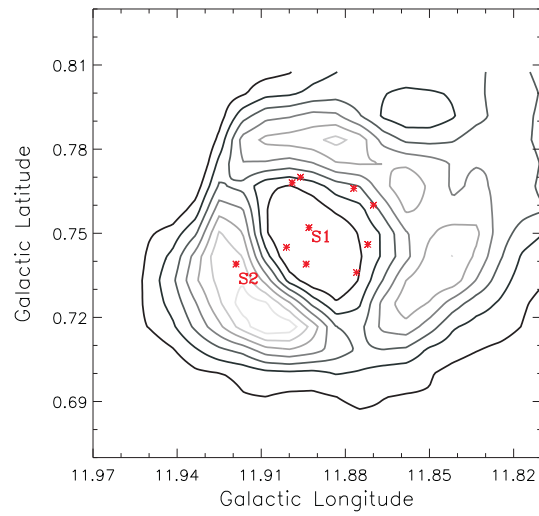
Fig. 9 Positions of massive stars overlaid on the^{13}CO $(1-0)$ integrated intensity contours. Contour levels start at 30% ($\sim$ 12 K km s^{-1}) of the peak ^{13}CO integrated intensity, with a step of $\sim$ 4 K km s^{-1}. The red asterisks are labeled as candidates of massive stars that we found. S1 and S2 are labeled as the targets we discuss in the paper.
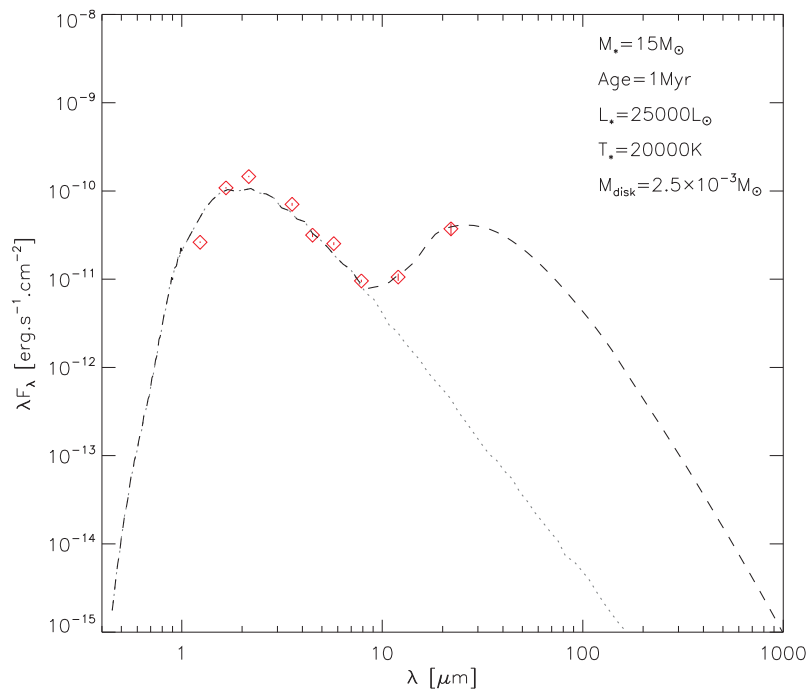
Fig. 10 The SED-fitting results of S1. The black dashed line represents the best-fitting model, whereas the stellar contribution to the total flux of the system is depicted as a grey dotted line. The observed data points are marked as diamonds (JHK + IRAC + WISE 12 µm + WISE 22 µm).

4.2 Triggered Star Formation in N4

Watson et al. (2010) analyzed the distribution of YSOs around several bubbles that have been identified in the mid-infrared, including N4. Several YSOs were identified inside the shell, along the shell, and outside the shell, but there is no clear peak in the distribution of YSOs in the N4 region.

They did not find any evidence of triggered star formation in N4. They claimed the reason may be that triggered star formation is difficult to identify there, either because of contamination in identifying YSOs or because the triggering mechanism does not dominate.

However, we may have found the evidence of triggered star formation in N4. As mentioned before, there exists the signature of infall motion in N4, implying a high-mass YSO is forming. According to the velocity structure and the distribution of CO in N4, we know that N4 is expanding. This process can result in interaction with the surrounding molecular clouds and trigger massive star formation near clumps in the shell. Therefore we believe that this forming YSO has been triggered by the expansion of N4.

Interestingly, a star labeled S2 in Figure 9, which is located above the dashed line in Figure 8, is selected as a candidate of a massive star, whose coordinate ($l = 11.92°$, $b = 0.74°$) is consistent with the infall candidate we have found. It suggests that S2 and the infall candidate are probably the same source. Since S2 is embedded in N4, we suggest that the formation process of S2 may have been triggered by the expansion of N4. Since the resolution of our observation is not good enough, higher resolution observations are needed to confirm this.

5 CONCLUSIONS

We have carried out simultaneous observations of the three CO ($J = 1-0$) (^{12}CO, ^{13}CO and C^{18}O) line emissions towards N4. Reviewing the CO data of N4, in conjunction with the GLIMPSE data, enables us to draw the following conclusions:

(1) The CO emissions are faint in the central regions of N4 and are clearly associated with the 8.0 μm emission; their morphologies are similar, especially the C^{18}O emission.
(2) The mass of N4 is $\sim 7.0 \times 10^3\ M_\odot$ (using ^{13}CO).
(3) N4 is more likely to be an inclined expanding ring than a spherical bubble.
(4) There exists the signature of infall motion in N4, which can be a good candidate to study the infall process. Star formation may have been triggered by the expansion of N4.
(5) S1 may be the energy source for the expansion of N4.

References

Arce, H. G., Borkin, M. A., Goodman, A. A., Pineda, J. E., & Beaumont, C. N. 2011, ApJ, 742, 105

Beaumont, C. N., & Williams, J. P. 2010, ApJ, 709, 791

Benjamin, R. A., Churchwell, E., Babler, B. L., et al. 2003, PASP, 115, 953

Bernasconi, P. A. 1996, A&AS, 120, 57

Castets, A., & Langer, W. D. 1995, A&A, 294, 835

Churchwell, E., Povich, M. S., Allen, D., et al. 2006, ApJ, 649, 759

Churchwell, E., Babler, B. L., Meade, M. R., et al. 2009, PASP, 121, 213

Covey, K. R., Ivezić, Ž., Schlegel, D., et al. 2007, AJ, 134, 2398

Deharveng, L., Schuller, F., Anderson, L. D., et al. 2010, A&A, 523, A6

Elmegreen, B. G., & Lada, C. J. 1977, ApJ, 214, 725

Keto, E. 2003, ApJ, 599, 1196

Liu, Y., Madlener, D., Wolf, S., Wang, H., & Ruge, J. P. 2012, A&A, 546, A7

Mardones, D., Myers, P. C., Tafalla, M., et al. 1997, ApJ, 489, 719

Nagahama, T., Mizuno, A., Ogawa, H., & Fukui, Y. 1998, AJ, 116, 336

Ren, Z., Wu, Y., Zhu, M., et al. 2012, MNRAS, 422, 1098

Rohlfs, K., & Wilson, T. L. 2000, Astronomische Nachrichten, 321, 274

Shan, W. L., Ji, Yang., Shi S. C., et al. 2012, IEEE, 2, 6

Skrutskie, M. F., Cutri, R. M., Stiening, R., et al. 2006, AJ, 131, 1163

Sollins, P. K., & Ho, P. T. P. 2005, ApJ, 630, 987

Watson, C., Povich, M. S., Churchwell, E. B., et al. 2008, ApJ, 681, 1341

Watson, C., Hanspal, U., & Mengistu, A. 2010, ApJ, 716, 1478

Wolf, S. 2003, Computer Physics Communications, 150, 99

Zhou, S., Evans, N. J., II, Koempe, C., & Walmsley, C. M. 1993, ApJ, 404, 232

Zuo, Y. X., Li, Y., Sun, J. X., et al. 2011, Acta Astronomica Sinica, 52, 152